



Dynamical Behavior of a Tensegrity Structure Coupled to a Spatial Steel Grid

Ángel Otoniel González Martínez¹, Jaime Moisés Horta Rangel^{1*},
Miguel Angel Perez Lara y Hernandez¹, Moises Arroyo Contreras¹,
Juan Bosco Hernandez Zaragoza¹, Luz Perez Rea¹, Teresa Lopez Lara¹
and Eduardo Rojas Gonzalez¹

¹Universidad Autónoma de Querétaro, Cerro de las Campanas, Querétaro, Querétaro 76010, México.

Authors' contributions

This work was carried out in collaboration among all authors. All authors read and approved the final manuscript.

Article Information

DOI: 10.9734/CJAST/2019/v38i230350

Editor(s):

(1) Professor Jerzy Nowacki PhD, DsC West Pomeranian University of Technology, Szczecin Institute of Materials Science and Engineering, Poland.

Reviewers:

(1) Marin Marin, Transilvania University of Brasov, Romania.
(2) J. Dario Aristizabal-Ochoa, Universidad Nacional de Colombia at Medellin, Colombia.
Complete Peer review History: <https://sdiarticle4.com/review-history/52005>

Original Research Article

Received 31 July 2019
Accepted 09 October 2019
Published 15 October 2019

ABSTRACT

Aim: In this study it is presented a methodology to determine the structural response of a tensegrity system working under the effects of wind, temperature variations and when coupled to a steel spatial grid applied as pedestrian bridge. This methodology is based in applying nonlinear static and dynamic analyzes and the base motion method.

Place and Duration of Study: The study was carried out in the Graduate Engineering Department, Universidad Autonoma de Queretaro, Queretaro, Mexico. September 2017 to July 2019.

Methodology: At first instance, it was analyzed the equilibrium configuration of a tensegrity system by only considering self-weight through non-linear static analyzes. In the second stage, it was studied the structural response and internal forces of the proposed tensegrity system under environmental loads as temperature variations and wind forces, which were represented as dynamic effects in a non-linear finite element model. Later, a spatial steel grid was analyzed for such environmental loads but using linear static analyzes. Finally, by applying the principle of

*Corresponding author: E-mail: horta@uaq.mx;

superposition to the spatial steel grid, and the base motion method to the tensegrity system, it was represented the coupling of both systems as a single assembly.

Results: The structural response of a tensegrity system when working under different load conditions is obtained. Also, the effects produced by the coupling of both systems are determined.

Conclusion: The study concluded that the tensegrity system shows a stable response for the different load combinations established. There are also denoted the increases in internal forces and displacements for specific loads cases, which may affect locally some components and the overall behavior of the assembly.

Keywords: Tensegrity structures; static and dynamic nonlinear analysis; base motion method; pedestrian bridge.

1. INTRODUCTION

Tensegrity structures (TS) are generally attractive to users, they have mechanical characteristics that in comparison to conventional systems, increase their structural efficiency (load bearing/self-weight ratio) [1–3]. TS allow the use of sustainable materials and the implementation of efficient constructive processes, because a large percentage of the structure is work-shop made, this minimizes the building time. TS are pin-jointed free-standing structures, made-up by a continuous red of cables working under tensile forces, in which, isolated bar elements, that works under compression forces are contained [4]. Initially proposed by R. B. Fuller, K. Snelson and G. Emmerich [1], their name is a contraction of the words “tensional integrity”, proposed by R. B. Fuller.

It is considered that the invention of TS was done in the plastic arts field [1]; however, in the architecture and civil engineering, many structural systems, partially based on the mechanical behavior of TS have been developed, such as the tensile membrane structures from La Plata stadium roof and the Georgia Dome [5]; another example is the Kurilpa bridge, which is claimed as the first hybrid TS implemented in an elevated pedestrian walkway [6].

In aerospace and robotics fields, TS are applied as folding structures and smart structures, due their capacity to change their shape, by controlling the prestress of cable elements [7]. The super ball-bot is one of the ultimate developments of these areas, it was created by NASA as a planetary exploration robot [8].

From a structural mechanics point of view, progress and knowledge about TS stand out. Current research proposes various techniques and methodologies to perform numerical models [9]. Behavior of TS adapted to work against

gravitational static loads has been analyzed by [10,11]. [5,12] studied TS under static and dynamic wind forces. In addition, modal parameters have been characterized considering variations in the ambient temperature of some common TS [13].

However, from the literature review, it is noted that, in current researches, little has been studied about the interaction of environmental effects and the multiple load combinations that would act on a TS exposed to outdoor conditions [14]. The integration of these variables can be carried out through dynamic non-linear methods, since they allow to approximate, to a greater degree, the behavior of TS under the above-mentioned weather load cases.

It should be noted, the null scope by the building codes, in regards to the analysis and design of tensegrity structures. This fact is one of the main aspects that limit the implementation of TS as civil structures [2,15]. In the absence of such regulations, researches carried out on these systems, define that stability is the parameter that allows describing the behavior of TS.

Historically, research about tensegrity systems has focused mainly on the finding form process [16], due to, in assemblies with complex geometries or large amounts of elements, not all the methods converge. Other reason is that current methods do not allow to control the resulting geometric characteristics, or, to keep the principle of mechanical unilaterality for each type of element [17–20]. Although it should be noted that the methods developed to date, are convenient and can be adapted or modified to solve a specific system.

It has been studied the characteristics and conditions to ensure stability of TS, considering self-weight and prestress of cables. Connelly [21] presents a criterion called “Super stability”, through which analyses basic prismatic systems.

Subsequently, [22] defines two concepts of stiffness for TS, that are named “Prestress stability” and “Second order stiffness”, by which, stability is provided to the TS. Similarly, Deng and Kwan [23] propose a general classification of the necessary conditions to determine the stability of an ET, by analyzing the tangential stiffness matrix and considering the variations of the potential energy of the second order. Complementing these works, Zhang and Ohsaki [24] formally establish the conditions required for an TS to be stable, which are based in the fact that the tangent stiffness matrix must be defined and positive. Their conclusions states that the minimum necessary conditions are: the force density matrix must be positive and defined, in addition to having a minimum range deficiency equal to $d+1$; and, the range of the geometric stiffness matrix should be $d(d+1)/2$ where d is the vector of non-trivial displacements.

Subsequently, TS structural response was characterized under the effects of external loads as compression, tension and torsion. Lazopoulos [25] employs the bifurcation method, to study the conditions that generate global and local instabilities in a 3-plex system. Amendola [26] studied the behavior of the 3-plex system, considering compressive loads for two boundary conditions cases at the base nodes: with total restriction of movement, and, with freedom of movement in the horizontal plane. From case 1, it is shown that the structure tends to stiffen when the load is applied, and for the second case, 3-plex systems presents a softening behavior. 3-plex system was also studied by Zhang et al. [27], who identified that, when acting torsional loads, a new type of instabilities appears which were named ‘Snapping Instabilities’. It was observed that this behavior was present in the transition of equilibrium states, once the system was loaded. Snapping instability occurs when torsional load is higher than the allowable, which generates permanent deformations, even when the elements work within the elastic limit. Atig et al. [28] discuss the possible existence of dynamic instabilities in the 3-plex system and in the Geiger dome. This effect was observed when systems were excited

with white noise, and is associated to slackening of cables during loading cycles.

The previously presented works identify that some systems may present instabilities caused by external loads. In addition, there is a lack of knowledge about the response of tensegrity systems applied in cases other than light-weight roofs, where the interaction of wind effects with temperature variations is included. Therefore, this work presents the study and development of a stable tensegrity system, under dynamic environmental loads. This tensegrity structure will be coupled to the superstructure of a pedestrian bridge, applying the “ground motion” method, in order to represent the behavior of whole assembly under the described external loads.

2. MATERIALS AND METHODS

2.1 Superstructure Description for the Proposed Pedestrian Bridge

Superstructure of the pedestrian bridge is composed by two different systems: the main structure of the bridge, which consist of a single-lattice spatial layer grid (also known as spatial double layer grid, SDLG), and by five identical tensegrity modules, which are the result of this research, and will be coupled to the main structure.

SPLG is integrated by the parts indicated in Fig. 1. It has a total length of 28.0 m, width of 2.80 m, and 1.50 m for height; covering a clear span of 22.0 m. It is proposed a floor system by precast W-deck panels whose weight is 200 kg/m^2 , and will be mounted on a steel support system, that will allow their installation. Per the Mexican standards for bridges [29] live load will be considered as 400 kg/m^2 . Table 1 shows the mechanical properties of the structural elements used for this system [30,31].

Fig. 2 shows a view in the X-Y plane, at a height of 0.0 m. This geometric configuration allows the coupling of the five tensegrity modules, whose location corresponds to the dotted areas of green and blue.

Table 1. Mechanical properties of the SDLG components

Cross-section type	Round HSS	Rectangular HSS	Round tubes
ASTM Standard	A500 Gr. 42	A500 Gr. 46	A53 Gr. B
Yield Stress (Fy)	2952 kg/cm ²	3234 kg/cm ²	2460 kg/cm ²
Ultimate Stress (Fu)	4077 kg/cm ²	4077 kg/cm ²	4218 kg/cm ²

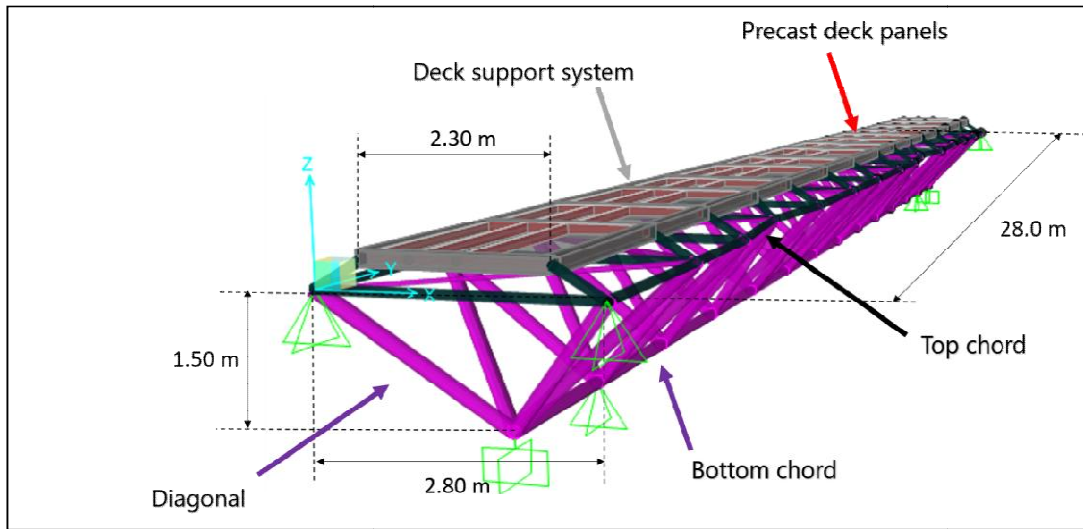


Fig. 1. 3D view of the SDLG

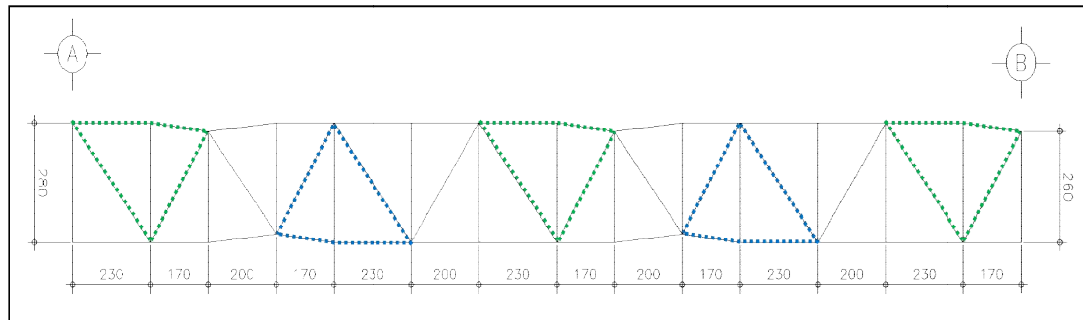


Fig. 2. View in the X-Y plane of the SDLG, Z = 0.0 m

The tensegrity module developed in this work is called "X-T". Topology and connectivity of the X-T module are described by Fig. 3. The X-T system consists of 27 elements, of which 5 elements are bar type and 22 elements are cable type, which converge to 10 nodes. This assembly was developed with the aim of establishing a tensegrity system, whose geometrical and architectural features allow pedestrian traffic, when implemented on a pedestrian bridge. The interior clearance of the X-T module (Fig. 4a and 4b) is 2.70 m wide and 2.80 m high. The total

width is 4.90 m, its length is 3.8 m and the total height is 5.45 m.

The spatial configuration of the X-T module was obtained by applying a form finding method based on the double decomposition of singular values, initially proposed by Yuan [18]. The nodal coordinates of this system are shown in Table 2, which were obtained from a previous work [32]. Additionally, in Table 3, the mechanical characteristics of the materials that make up this system are shown [33,34].

Table 2. Nodal coordinates

Node	X	Y	Z	Node	X	Y	Z
1	0.000	0.000	0.000	6	2.800	2.300	0.000
2	0.000	3.800	3.800	7	2.261	-0.829	2.500
3	0.200	0.000	3.900	8	2.261	4.829	2.500
4	0.200	4.000	0.000	9	-1.300	2.200	2.000
5	1.336	2.000	5.464	10	3.613	2.200	3.146

Table 3. Mechanical properties of the tensegrity components

Element type	Bar	Cable
ASTM Nom.	Aluminum 6063 T6	A586 Class A.
Modulus of elasticity kg/cm^2	710,100.3	1687,367.1
Yield Stress (F_y) kg/cm^2	1,757.67	10,546
Ultimate Stress (F_u) kg/cm^2	2,109.21	15,467.5

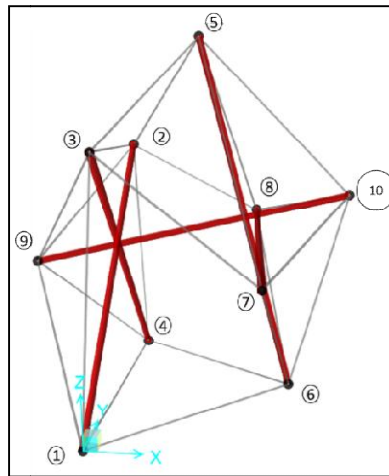


Fig. 3. Perspective view and node numbering of the X-T module

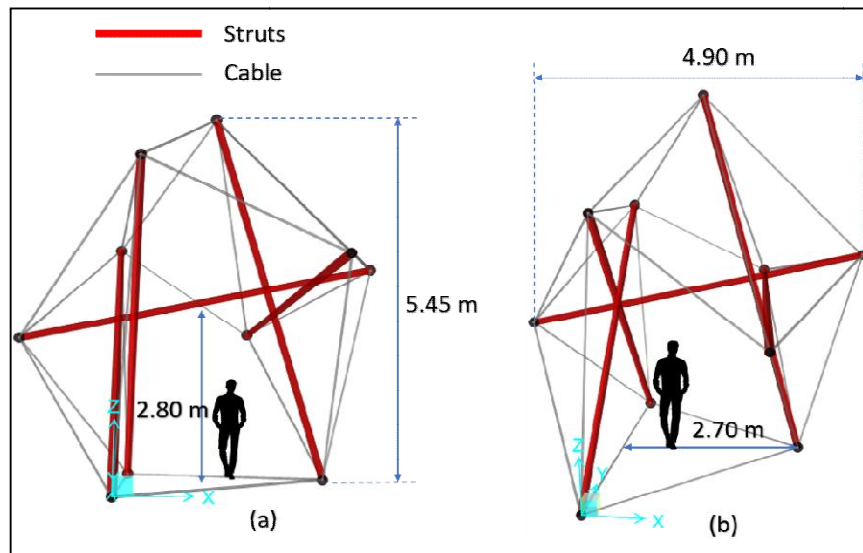


Fig. 4. External and internal dimensions of the X-T module

2.2 Mathematical Framework

Several authors have investigated and contributed to determine the mathematical models that represent the mechanical behavior of tensegrity structures [35,36]. Murakami [10,11] shows in detail the basic equations for static and

dynamic analyzes, both in Eulerian and Lagrangian formulations. Mechanical principles that must be met, refer in particular to the equilibrium the system, compatibility between displacements and deformations, and the relationships between internal and external forces. These conditions, which are actually

general for any mechanical system, can be stated in tensorial expressions as follows [37]:

a) Equilibrium equation

$$\text{Div}\tilde{S} + \underline{b} = \rho \dot{v} \quad (1)$$

b) Strain-Displacement Relation

$$\tilde{E} = \frac{1}{2}(\nabla \underline{u} + \nabla \underline{u}^T) \quad (2)$$

c) Strain-Stress Relation (Compatibility equation)

$$\tilde{S} = \tilde{C} = 2\mu\tilde{E} + \lambda(\text{tr}\tilde{E})\tilde{I} \quad (3)$$

Where:

\tilde{E} : Deformation tensor. Second-order tensor formed as:

$$\tilde{E} = \sum_{i,j} E_{ij} e_i \otimes e_j \quad (4)$$

\tilde{C} : Elasticity tensor. Fourth-order tensor.

\tilde{I} : Identity tensor.

\tilde{S} : Piola-Kirchhoff stress tensor. Second-order tensor.

$\nabla \underline{u}$: Deformation gradient

\underline{b} : Body forces field

ρ : Density field

\dot{v} : Acceleration field

μ, λ : Lamé parameters

2.3 Finite Element Method

Tensegrity structures have a non-linear behavior when working under external loads, because, both the stiffness of the system and the loads, are in function of displacements and / or deformations, which are generally of great magnitude in such type of systems. On the other hand, prestress of cable elements generates a non-linear geometric effect on the system [38]. In this work, only the nonlinear geometric effects in the elastic range of the cable elements will be considered.

Finite element method (MEF) is a numerical procedure used to find an approximate solution of partial differential equations that allow modeling a physical system. The discrete model associated to the mechanical behavior of a system, described in terms of the stiffness method is [39]:

$$\left\{ \int_V [B]^T [D] [B] dV + \int_V [G]^T [M] [G] dV \right\} \{U\} = \int_V [N]^T \begin{Bmatrix} b_x \\ b_y \\ b_z \end{Bmatrix} dV + \int_V \{\varepsilon_0\}^T [D] \{\varepsilon_0\} dV + \begin{Bmatrix} F_x \\ F_y \\ F_z \end{Bmatrix} \quad (5)$$

where [B] is the derivations shape functions matrix, [E] is the elastic constants matrix, [G] is the partial derivations shape functions matrix, [M] is the membrane forces matrix, {U} is the nodal displacement vector, [N] is the shape functions matrix, {bx by bz}^T is the body forces vector, {ε₀} is the vector of residual stresses associated with temperature variation and {F_x F_y F_z}^T is the vector of nodal external forces.

The mathematical model of equation (5) can be represented in simplified form as:

$$[K_t]\{U\} = \{[K] + [K_G]\}\{U\} = \begin{Bmatrix} W_x \\ W_y \\ W_z \end{Bmatrix} + \begin{Bmatrix} \varepsilon_x \\ \varepsilon_y \\ \varepsilon_z \end{Bmatrix} + \begin{Bmatrix} F_x \\ F_y \\ F_z \end{Bmatrix} \quad (6)$$

where [K_t] is the tangent stiffness matrix, [K] is the elastic stiffness matrix, [K_G] is the geometrical stiffness matrix, {W_x W_y W_z}^T is the force vector associated to the self-weight of each element, and {ε_x ε_y ε_z}^T is the vector of residual forces related with temperature variations [40–42].

2.4 Static Nonlinear Analysis

The solution of the TS will be carried out applying an iterative-incremental method for nonlinear structural analysis, called Newton-Raphson [43]. In terms of FEM, the equations system is expressed as:

$$[K_t]\Delta\{U\}^j = \begin{Bmatrix} W_x \\ W_y \\ W_z \end{Bmatrix} + \begin{Bmatrix} \varepsilon_x \\ \varepsilon_y \\ \varepsilon_z \end{Bmatrix} + \begin{Bmatrix} F_x \\ F_y \\ F_z \end{Bmatrix} \quad (7)$$

where Δ represents the variations at the “j” iteration in the displacement vector {U}.

For bar elements, where only act axial effects, the stiffness matrices are structured as follows:

$$[K] = \left(\frac{EA}{L} \right) \begin{bmatrix} 1 & 0 & 0 & -1 & 0 & 1 \\ 0 & 0 & 0 & 0 & 0 & 0 \\ 0 & 0 & 0 & 0 & 0 & 0 \\ -1 & 0 & 0 & 1 & 0 & -1 \\ 0 & 0 & 0 & 0 & 0 & 0 \\ 0 & 0 & 0 & 0 & 0 & 0 \end{bmatrix} \quad (8)$$

$$[K_G] = \left(\frac{T}{L}\right) \begin{bmatrix} 1 & 0 & 0 & -1 & 0 & 0 \\ 0 & 1 & 0 & 0 & -1 & 0 \\ 0 & 0 & 1 & 0 & 0 & -1 \\ -1 & 0 & 0 & 1 & 0 & 0 \\ 0 & -1 & 0 & 0 & 1 & 0 \\ 0 & 0 & -1 & 0 & 0 & 1 \end{bmatrix} \quad (9)$$

where E is the modulus of elasticity of the material, A is the cross-sectional area of each element, L is the length of the element and T is the internal membrane force, that is naturally associated with prestress of the cable elements.

2.5 Dynamic nonlinear analysis

Nonlinear dynamic models will be used to represent the effects of wind and the coupling of tensegrity systems with the SDLG, such as forces and displacements as a function of time. The characteristic equation for the dynamic equilibrium problems is:

$$[M]\{\ddot{U}\}_{n+1}^j + [C]\{\dot{U}\}_{n+1}^j + [K_t]\{U\}_{n+1}^j = P(t) \quad (10)$$

with $P(t)$ defined as:

$$P(t) = \begin{Bmatrix} W_x \\ W_y \\ W_z \end{Bmatrix}_{n+1} + \begin{Bmatrix} \varepsilon_x \\ \varepsilon_y \\ \varepsilon_z \end{Bmatrix}_{n+1} + \begin{Bmatrix} F_x \\ F_y \\ F_z \end{Bmatrix}_{n+1}^j \quad (11)$$

where $[M]$ is the mass matrix, $\{\ddot{U}\}$ is the vector of acceleration, $[C]$ is the damping matrix, $\{\dot{U}\}$ is the velocity vector. "n" represents the current incremental step and "j" represents the next incremental step [44].

2.5.1 Pulse-type excitation function

Particularly, the force of the wind acting on the structure will be represented with a pulse-type excitation function, with the aim of idealizing a gust of wind that will act for an interval $t = 4$ s, and then cease. Fig. 5 shows the diagram of the proposed function to model the wind gust [44].

Considering the initial conditions $\mathbf{u}(0) = 0$, $\mathbf{y}\dot{\mathbf{u}}(0) = 0$, with a value damping of 2.4%, the solution for this type of excitation is:

$$u(t) = \frac{P_0}{k} \left[1 - e^{-\zeta\omega_n t} \left(\cos(\omega_d t) + \frac{\zeta\omega_n}{\omega_d} \sin(\omega_d t) \right) \right] \quad (12)$$

2.5.2 Newmark-beta method of direct integration

Direct integration methods are used to solve initial value problems by a step-by-step integration with respect to time [44,45]. It is assumed that both displacements $\{U\}$ and velocities $\{\dot{U}\}$ are known at a given time $t = 0$ s. The solution obtained with this method is given through an incremental approximation process.

Newmark-Beta method states that, considering the mean value theorem, the first derivative of displacement, can be solved as:

$$\dot{u}_{n+1} = \dot{u}_n + \Delta t \ddot{u}_y \quad (13)$$

where:

$$\ddot{u}_y = (1 - \gamma)\ddot{u}_n + \gamma\ddot{u}_{n+1} \quad (14)$$

with $0 < \gamma < 1$. Thus:

$$\dot{u}_{n+1} = \dot{u}_n + \Delta t ((1 - \gamma)\ddot{u}_n + \gamma\ddot{u}_{n+1}) \quad (15)$$

Since acceleration also varies over the time, the average value theorem will be used again to calculate the second derivative of the displacement.

$$u_{n+1} = u_n + \Delta t \dot{u}_n + \frac{1}{2} \Delta t^2 \ddot{u}_\beta \quad (16)$$

with $0 < 2\beta < 1$. In this way:

$$\ddot{u}_\beta = (1 - 2\beta)\ddot{u}_n + 2\beta\ddot{u}_{n+1} \quad (17)$$

For this method a value of 0.5 for γ and 0.25 for β are suggested, which gives stability to the method. Which is expressed as:

$$\dot{u}_{n+1} = \dot{u}_n + \frac{\Delta t}{2} (\ddot{u}_n + \ddot{u}_{n+1}) \quad (18)$$

$$u_{n+1} = u_n + \Delta t \dot{u}_n + \frac{1 - 2\beta}{2} \Delta t^2 \ddot{u}_n + \beta \Delta t^2 \ddot{u}_{n+1} \quad (19)$$

2.5.3 Base motion method

When the supports of a structural system produce or transmit actions to the structure, as manner of movement (Fig. 6), it is convenient to propose equation (10), in function on the relative displacements as follows [44,45]:

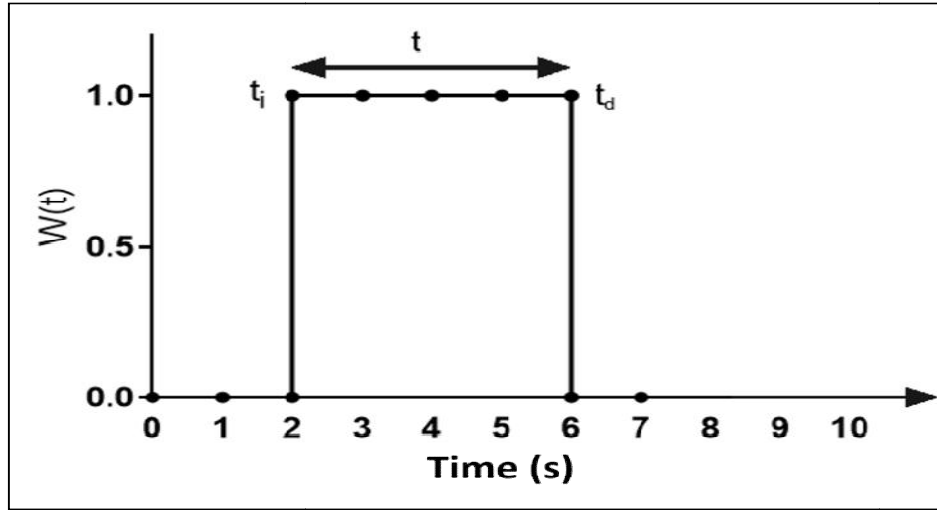


Fig. 5. Pulse-type excitation function

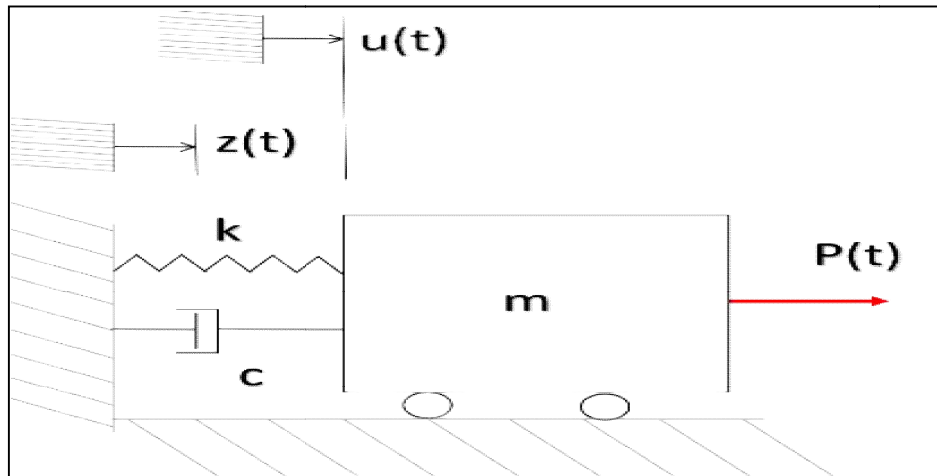


Fig. 6. Representative system of the base motion method

$$\begin{aligned}
 [M]\{\ddot{U}\}_{n+1}^j + [C]\{\dot{U} - \dot{Z}\}_{n+1}^j \\
 + [K_t]\{U - Z\}_{n+1}^j \\
 = P(t)
 \end{aligned}
 \quad (20)$$

Expressing Eq. (20) as a relative displacements $W = U - Z$, $\dot{W} = \dot{U} - \dot{Z}$ and $\ddot{W} = \ddot{U} - \ddot{Z}$, results:

$$\begin{aligned}
 [M]\{\ddot{W}\}_{n+1}^j + [C]\{\dot{W}\}_{n+1}^j + [K_t]\{W\}_{n+1}^j \\
 = P(t) - [M]\{\ddot{Z}\}_{n+1}^j
 \end{aligned}
 \quad (21)$$

2.6 Methodology

In the first instance, non-linear static analyzes of the tensegrity system were carried out, in the software SAP2000 [46], to determine the spatial configuration and internal axial forces associated

with the equilibrium of the system under gravitational effects. The boundary conditions of the support nodes are shown in Table 4.

It is considered that the pedestrian bridge will be located in Queretaro, Mexico. For this site it is estimated a wind speed for design of 101.8 km/hr and a wind pressure of 77.83 kg/m² [47]. The maximum average temperature in summer is 31°C and in winter it is 23.3°C; while the minimum average temperature in summer is 15°C and in winter it is 7°C [48]. Therefore, two cases of thermal variation will be analyzed, an increase of 16°C and a decrease of 16°C.

Both structures were analyzed with independent finite element models, applying the Mexican

standards for design of pedestrian bridges [47]. Load combinations for the SDLG analysis are shown in Table 5. For service and work load combinations, the coefficient ζ is equal to 1, while for design combinations it will have a value of 1.25 for CT-2 and CT-3 cases, and, equal to 1.40 for CT-5 y CT-6 cases. The value of γ is equal to 1 service load combinations. On the other hand, for design combinations, this coefficient will take a value of 1.30 for FC-2 y FC-3, and, 1.25 for FC-5 y FC-6 cases.

Nomenclature of the loads shown in Table 5 is: DL = Dead load, LL = Live load, W = Wind force on the structure, WLL = Wind over the live load, and, T = Temperature. β_{CM} is equal to 1.0 for bending and pure tension elements. While, for elements working under bending and compression simultaneously, there are the following cases: $\beta_{CM} = 1.0$, for the condition of maximum axial load and minimum bending moment; $\beta_{CM} = 0.75$, for the condition of minimum axial load and maximum bending moment.

Load combinations for the TS are shown in Table 6.

Table 4. Boundary conditions of base nodes

Node	Ux	Uy	Uz
1	Fixed	Fixed	Fixed
4	Fixed	Free	Fixed
6	Fixed	Free	Fixed

Where "Sw" refers to self-weight, "Press" to the prestress in cables, and W to the wind load

acting over the structure. These load cases are described below:

In the load comb. 1, the structure was subjected to dynamic wind forces and temperature was considered constant ($\Delta T=0^{\circ}\text{C}$). At load combinations of group 2, it was first induced a 16°C ($\Delta T=+16^{\circ}\text{C}$) increase in temperature (comb. 2.a) and subsequently, the wind forces were applied as a dynamic function (comb. 2.b). Similarly, for the load combinations of group 3, it was considered a 16°C ($\Delta T=-16^{\circ}\text{C}$) decrease in temperature (comb. 3.a), prior to the application of wind forces on the system (comb. 3.b).

Analysis of SDLG was performed based on linear static models, where loads were idealized as constants. On the other hand, for TS, analyses were carried out by nonlinear static and dynamic models (see sections 2.4 and 2.5).

Once the internal forces, reactions and maximum nodal displacements of each system were determined, the actions between both systems were transferred. It was identified that the TS transfers loads to the SDLG, through its support nodes, effect that was represented by the superposition principle. In contrast, at those nodes of the SDLG, which join with the base nodes of TS, there were observed differential displacements, which were modeled as a dynamic problem of base motion.

The load cases, load combinations and the methodology presented throughout current section, were used to compute the mathematical models of both structural systems by means of SAP2000 software [46].

Table 5. Load combinations for SDLG

Service and work load combinations		Design load combinations	
CT-2	$\zeta^* (W)$	FC-2	$\gamma^* (\beta_{CM}DL + W)$
CT-3	$\zeta^* (DL + Sw + LL + 0.3W + WLL)$	FC-3	$\gamma^* (\beta_{CM}DL + Sw + 1.2LL + 0.3W + WLL)$
CT-5	$\zeta^* (DL + Sw + W + T)$	FC-5	$\gamma^* (\beta_{CM}DL + Sw + W + T)$
CT-6	$\zeta^* (DL + Sw + LL + 0.3W + WLL + T)$	FC-6	$\gamma^* (\beta_{CM}DL + 1.2LL + 0.3E + WLL + T)$

Table 6. Load combinations for the tensegrity structure

Load combination	
Comb. 1	$\zeta^* (Sw + Press + W)$
Comb. 2.a	$\zeta^* (Sw + Press + D16^{\circ}\text{C})$
Comb. 2.b	$\zeta^* (Sw + Press + D16^{\circ}\text{C} + W)$
Comb. 3.a	$\zeta^* (Sw + Press - D16^{\circ}\text{C})$
Comb. 3.b	$\zeta^* (Sw + Press - D16^{\circ}\text{C} + W)$

3. RESULTS AND DISCUSSION

The spatial configuration of the X-T module and the initial prestress values were obtained through the form finding process proposed by [18], which are the initial parameters to perform the nonlinear static analysis. Using the software SAP2000 [46], based on the finite element method, the results shown below were obtained.

3.1 Static Nonlinear Analysis under Self-Weight (Sw)

Static nonlinear analysis when only considering self-weight load case (Sw) of the X-T, module gives as result the spatial configuration shown in Table 7 (Fig. 7) and the axial forces from Table 8 and 9, in the column "Sw".

By comparing the nodal coordinates of Table 7 against the resulting coordinates of the search process so (see Table 2), it is observed that the higher order difference is 0.39 cm in the X axis at the node 7.

The maximum variation of axial force for bar elements occurs in the element 1, with an increase of 47 kg, equivalent to 4.7%. In cable elements, the maximum increase occurs in element 21, with a value of 30 kg, corresponding to an increase of 22.6%.

3.2 Structural Response and Internal Forces Variations of the "X-T" Module, due Dynamic Meteorological Actions

To study the behavior of the X-T module under the load combinations defined in Table 6, dynamic non-linear models were performed, with the aim of determining if the structural system is stable under these working conditions.

In the first instance the effects produced in some representative elements of the system are described below. For this, the axial force time-history graphs of bar 3 (Figs. 8 and 11), cable 18 (Figs. 9 and 12) and cable 19 (Figs. 10 and 13) are presented, in addition to the columns of load combination groups 1, 2 and 3, at Tables 8 and 9. The initial value of the axial force of the time history records corresponds to the axial force resulting from static nonlinear analysis from section 3.1. From $t = 0$ s to $t = 2$ s, the system is in equilibrium; from $t = 2$ s to $t = 6$ s, is the excitation period; and $t = 6$ s onwards is the free vibration period (see Fig. 5).

The results from combination 1, correspond to the effects of self-weight, prestressing and wind action. It is observed that, during the excitation period, the axial force on bar 3 (Fig. 8) increases up to 2450 kg, when the wind acts in the X

Table 7. Resulting nodal coordinates of the X-T module from a static nonlinear analysis considering self-weight

Node	X	Y	Z	Node	X	Y	Z
1	0.000	0.000	0.000	6	2.800	2.301	0.000
2	-0.004	3.801	3.799	7	2.257	-0.828	2.499
3	0.196	0.000	3.899	8	2.284	4.877	2.525
4	0.200	4.001	0.000	9	-1.302	2.200	1.998
5	1.332	2.000	5.463	10	3.610	2.200	3.146

Table 8. Maximum axial compression forces of bar elements for self-weight analysis and for the load combination groups 1, 2 and 3

Bar	Sw. Axial force (kg)	Load comb. 1 (DT=0°C)			Load comb. group 2 (DT=+16°C)			Load comb. group 3 (DT=- 16°C)		
		Wind effects			Thermal effects			Thermal + Wind effects		
		Axial force(kg)	DWD	Axial force(kg)	Axial force(kg)	DWD	Axial force (kg)	Axial force(kg)	DWD	
1	1047	1369	Yn	1663	2002	Yn	423	1263	X	
2	834	1044	Y	1337	1560	Y	317	969	X	
3	804	2450	X	1541	2422	X	177	2357	X	
4	639	1022	Xn	1164	1543	Xn	152	875	Xn	
5	418	1091	X	916	1110	Xn	123	1101	X	

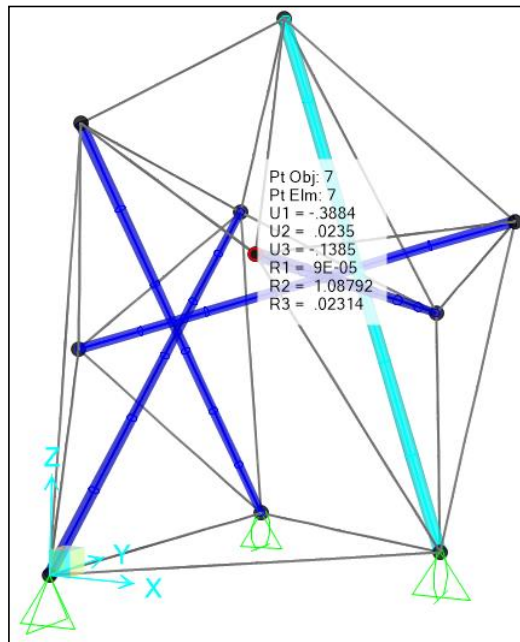


Fig. 7. Spatial configuration of X-T module under self-weight effects

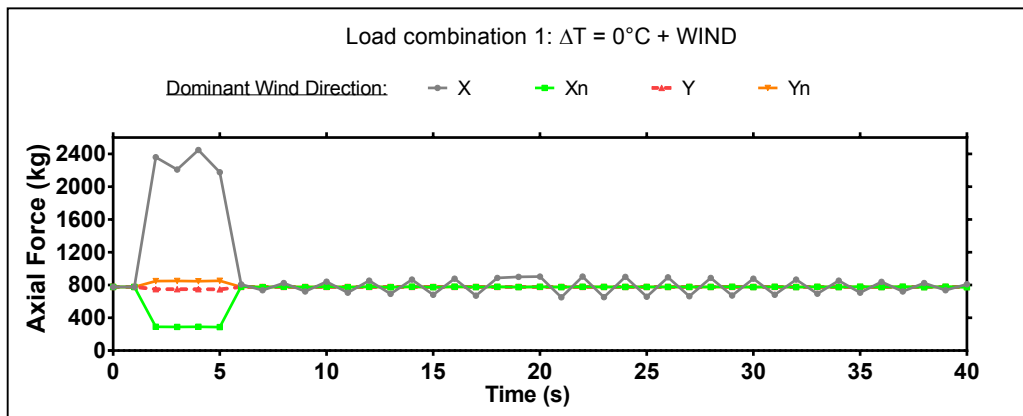


Fig. 8. Time-history record of axial force for bar 3, load combination 1

direction. In the free vibration period, residual oscillations of axial force are observed, in a range of +/- 100 kg, which are the product of the internal equilibrium processes of the tensegrity system, and show a decreasing trend over time.

Similar behavior is observed for cables 18 and 19, since, during the excitation period, the axial force increases to 1194 kg (Fig. 9) and 1109 kg (Fig. 10), respectively. However, it is observed that, in the cable 19, when the wind acts the negative X direction (Xn), the axial force is reduced to 0 kg. Subsequently, in the period of free vibration, it is observed that when the external effects culminate, the system has the

ability for each element to recover the axial force in equilibrium. For both elements, observed oscillations shown a decreasing tendency of axial force, from +/- 50 kg and +/- 70 kg, to 0 kg, respectively.

In the load combinations 2.a and 3.a, the effects of self-weight, prestress and thermal variation are related. Overall, with the exception of cables 26 and 27, it was recorded that, due to an increase in temperature, the axial force of the elements increases, because of volumetric expansion. In contrast, when temperature decreases, the axial force is reduced, given the contraction that is caused in the structural

elements. For cables 26 and 27, an inverse behavior is observed to that described previously, since, under an increase in temperature, the tension of cables 26 and 27 decreases, whereas, when a temperature decrease occurs, their axial force increases.

The results generated by combining the thermal variations together with the wind action, the effects of the own weight and the prestressing (combos 2.b and 3.b) are presented below.

For bar 3 (Fig. 11) corresponding to the load combination 2.b, it is observed that the axial force increases to 2422 kg, whereas, for the load combo 3.b, compression on bar 3 reaches a value of 2357 kg. In the free vibration period, it is observed that the oscillations of axial force are reduced to a range of 5 kg, for combination 2.b, and to 15 kg for the case 3.b, which decreases with time.

For cables 18 and 19, in the load combination 2.b, there are increases of the tensile forces up to 1163 kg and 1060 kg. While, in the load combo 3.b, axial forces of 1205 kg (Fig. 12) and 1119 kg (Fig. 13) are reached, respectively. Within the load combo 2.b, the oscillations of axial forces are reduced to a range of 5 kg for both elements; while in the case 3.b, the range of oscillations is reduced to 20 kg. In both load combinations, the tendency of oscillations is decreasing.

The behavior described previously, can be generalized for most of the components of the assembly, and the axial forces acting on each element are shown in Tables 8 and 9, in the columns for load combinations groups 2 and 3. From these results, it is highlighted that the maximum axial force to which each element is subjected, is caused by a specific wind direction, which will be named dominant wind direction (DWD). In addition, a temperature increase (combo 2.a) can produce a rise in axial forces up to 737 kg in the bar-type elements, and 398 kg in the cable elements; and the decrease in temperature (combo 3.a) produces variations of -627 kg in the bars and -356 kg in the cables. The inclusion of thermal variations together with the action of the wind produces variations of up to 851 kg in the cables and 1618 kg in the bars for the load combination 2.b. In the combination 3.b, the maximum variation is 1553 kg in the bar-type elements and 913 kg in the cables.

On the other hand, the registered nodal displacements from the dynamic analyzes are shown in Table 10. It is observed that the greatest displacements occur in the load combination 3.b, with a magnitude of 6.74 cm, at the free node 7, and of -0.34 cm for the base node 4.

Since node 7 has the largest displacements in the system, the time-history records generated from this node will be analyzed for the load combinations studied. From the time-history record of combo 1, it is observed that the greatest displacements occur during the excitation period in the X direction, up to 3.92 cm (Fig. 14); while, in the free vibration period, the node oscillates in a range of 0.1 cm, with a decreasing tendency around the equilibrium position. For the load combo 2.b, the displacement of the node is reduced to 0.43 cm, with oscillations around the equilibrium position of 0.1 cm. Whereas, the maximum recorded displacement occurs in the load combo 3.b, with a magnitude of 6.74 cm, where the vibrations reach a distance of 1 cm, and subsequently tend to decrease. The free nodes and the remaining support nodes, presents an analogous behavior, with minor displacements and vibrations (Fig. 15).

3.3 Spatial Double Layer Grid Behavior

Superstructure of the pedestrian bridge (SDLG) was modeled as a pin-jointed spatial system (see section 2.1) considering the loading conditions described in Table 5, and, idealizing its behavior as a linear static system. Given these characteristics, the proposed system presents the modal behavior of Table 11.

Mode 1 presents a frequency of 5.49 Hz, and a period of 0.182 s, corresponding to the horizontal direction X. Mode 2 has a frequency of 8.81 Hz and a period of 0.113 s, relative to the vertical direction Z, while the mode 11, with a frequency of 33.49 Hz and a period of 0.030 s, is associated with the horizontal direction Y. AASHTO [49] establishes that pedestrian bridges should be designed with a fundamental frequency in the vertical direction greater than 3 Hz, and in the horizontal direction, the frequency must be higher than 1.3 Hz. Thus, structural system is less likely to exhibit resonance effects and it is provided comfort to pedestrian users.

Displacements of the SDLG, for each combination of service loads, are shown in table

12. According to AASHTO (40)), vertical displacements must not exceed $L/360$, equivalent to 6.11 cm in the analyzed bridge, while, horizontal displacements should be less than $L/220$, corresponding to 10 cm. The SDLG presents a maximum vertical displacement of -2.34 cm at the clear span (Fig. 16), whereas, in the horizontal direction, the maximum displacement is -0.64 cm. These values are within the permissible limits by service conditions.

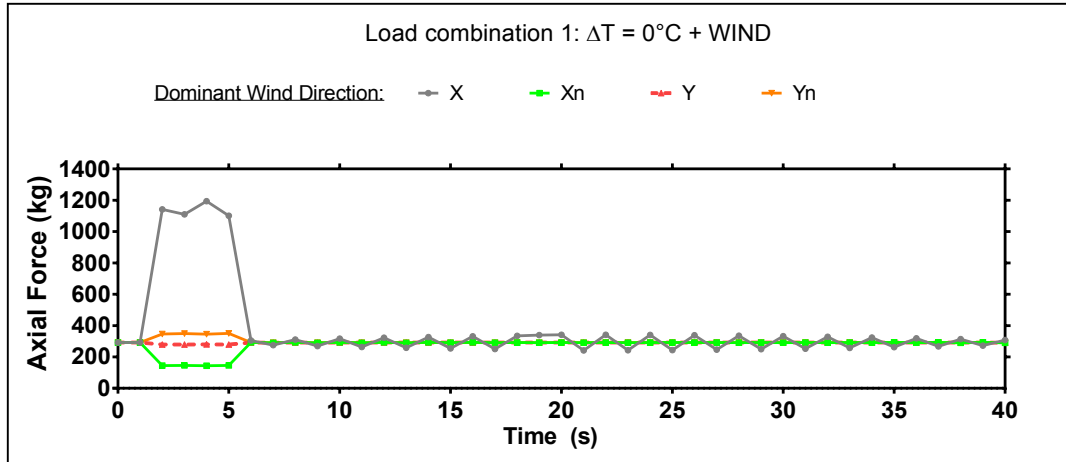


Fig. 9. Time-history record of axial force for cable 18, load combination 1

Table 9. Maximum axial tension forces of cable elements for self-weight analysis and for the load combination groups 1, 2 and 3

Sw.	Load comb. 1 (DT=0°C)			Load comb. group 2 (DT=+16°C)			Load comb. group 3 (DT=-16°C)		
	Axial force(kg)	Axial force(kg)	DWD	Thermal effects	Thermal + Wind effects	WDD	Thermal effects	Wind effects	DWD
6	472	662	Y	782	963	Yn	116	354	Y
7	501	675	X	747	937	Y	191	640	X
8	458	624	Xn	588	774	Xn	211	359	Xn
9	505	677	X	771	921	X	183	652	X
10	263	594	X	445	620	X	54	544	X
11	377	653	X	697	804	Xn	67	581	X
12	371	629	X	677	779	Xn	64	563	X
13	280	618	X	470	639	X	52	544	X
14	298	566	X	566	680	Yn	96	600	X
15	414	868	X	812	950	Yn	141	896	X
16	121	500	X	346	489	Y	25	502	X
17	71	365	X	346	489	Y	25	502	X
18	292	1194	X	676	1143	X	77	1205	X
19	221	1109	X	552	1060	X	35	1119	X
20	164	557	Xn	309	689	Xn	61	547	Xn
21	182	585	Xn	347	734	Xn	67	574	Xn
22	75	282	Xn	152	348	Xn	29	283	Xn
23	94	327	Xn	192	411	Xn	36	326	Xn
24	149	631	X	336	614	X	35	640	X
25	115	508	X	268	485	X	22	505	X
26	96	253	Y	6	181	Y	175	347	Y
27	107	201	Yn	2	200	Yn	199	261	Xn

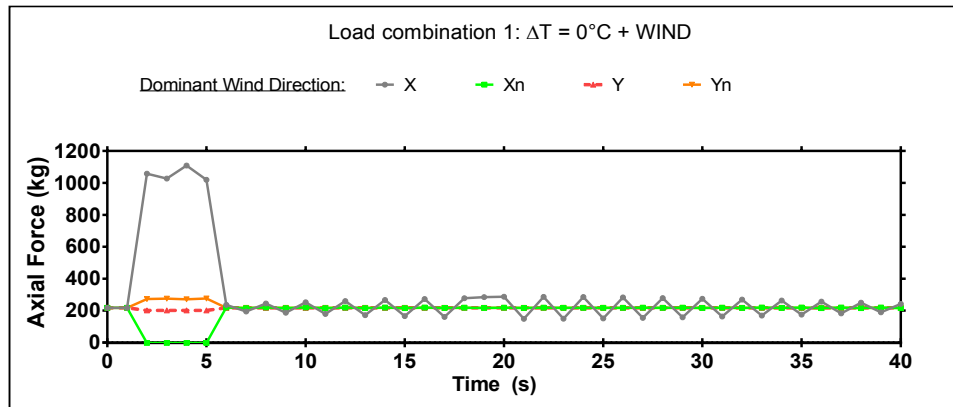


Fig. 10. Time-history record of axial force for cable 19, load combination 1

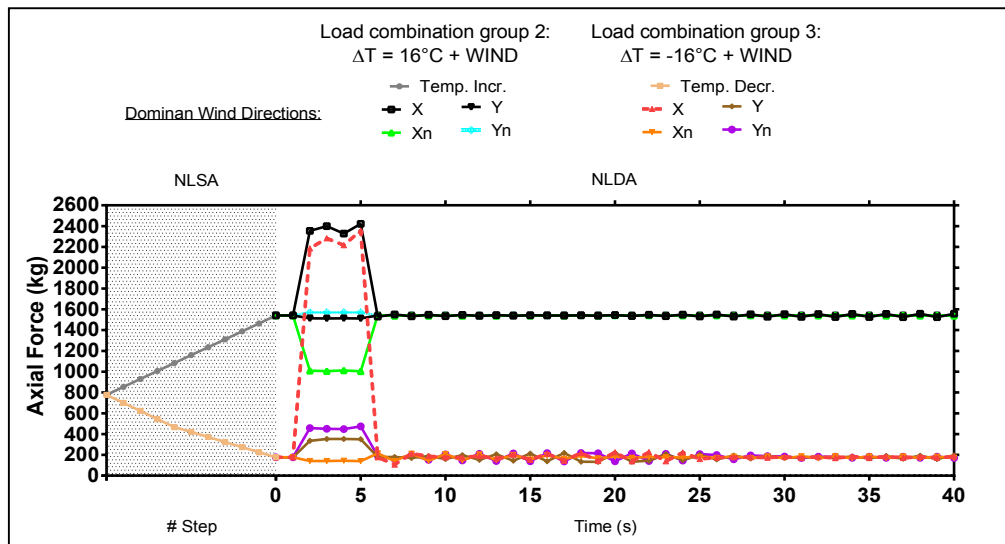


Fig. 11. Time-history record of axial force for bar 3, load combinations groups 2 and 3

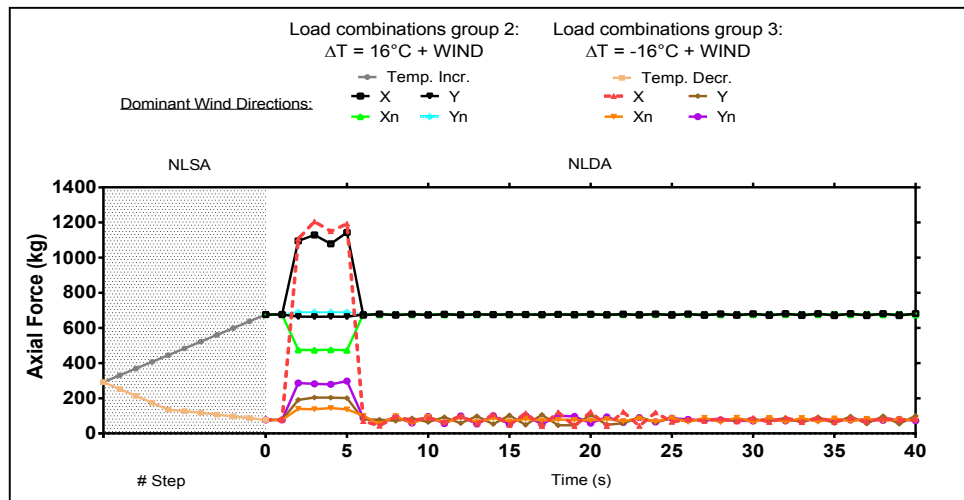


Fig. 12. Time-history record of axial force for cable 18, load combinations groups 2 and 3

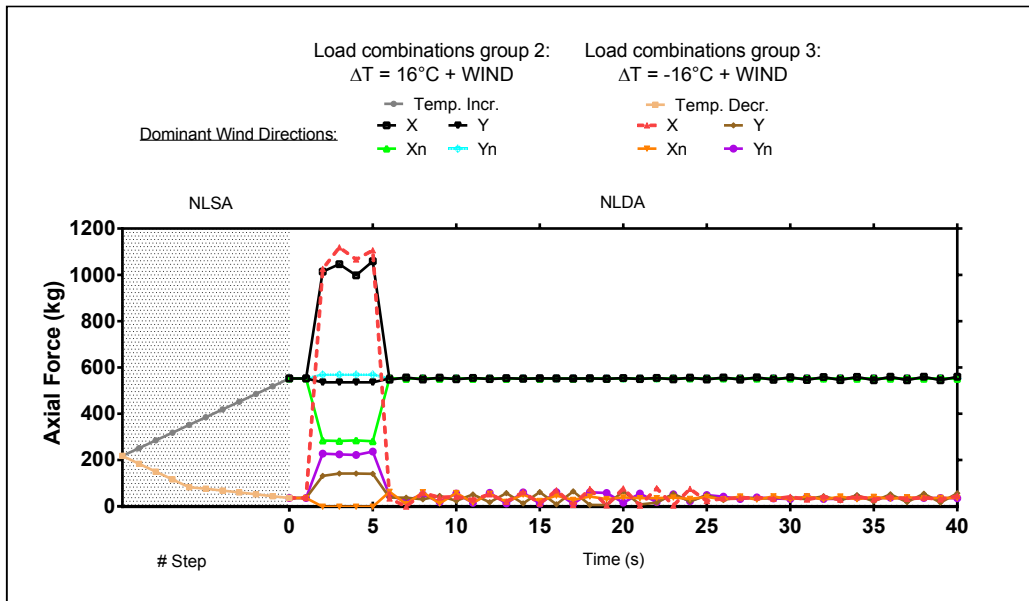


Fig. 13. Time-history record of axial force for cable 19, load combinations groups 2 and 3

Table 10. Maximum nodal displacements for the load combinations 1, 2.b and 3.b

Node	Case 1 (DT=0°C)				Case 2.b (DT=+16°C)				Case 3.b (DT=-16°C)			
	Wind effects				Thermal + Wind effects				Thermal + Wind effects			
	DX (cm)	DY (cm)	DZ (cm)	DWD	DX (cm)	DY (cm)	DZ (cm)	DWD	DX (cm)	DY (cm)	DZ (cm)	DWD
2	3.23	-0.19	0.19	X	1.25	0.17	0.22	X	5.57	-0.53	0.24	X
3	3.29	-0.13	-0.14	X	1.18	0.08	0.15	X	5.74	-0.19	-0.35	X
4	-	-0.05	-	Yn	-	0.18	-	Y	-	-0.34	-	Yn
5	2.68	-0.3	0.63	X	1.07	0.2	0.43	X	4.68	-1.07	0.93	X
6	-	-0.07	-	Yn	-	0.13	-	Xn	-	-0.26	-	Yn
7	3.92	-0.16	0.76	X	-0.43	-0.21	0.21	X	6.74	-0.49	1.25	X
8	3.66	-0.16	1	X	1.44	0.27	0.49	X	6.23	-0.77	1.62	X
9	1.59	-0.08	1.19	X	0.59	0.1	0.50	X	2.75	-0.19	1.96	X
10	1.93	-1.35	-0.4	X	0.88	-0.38	0.14	X	3.17	-2.46	-0.82	X

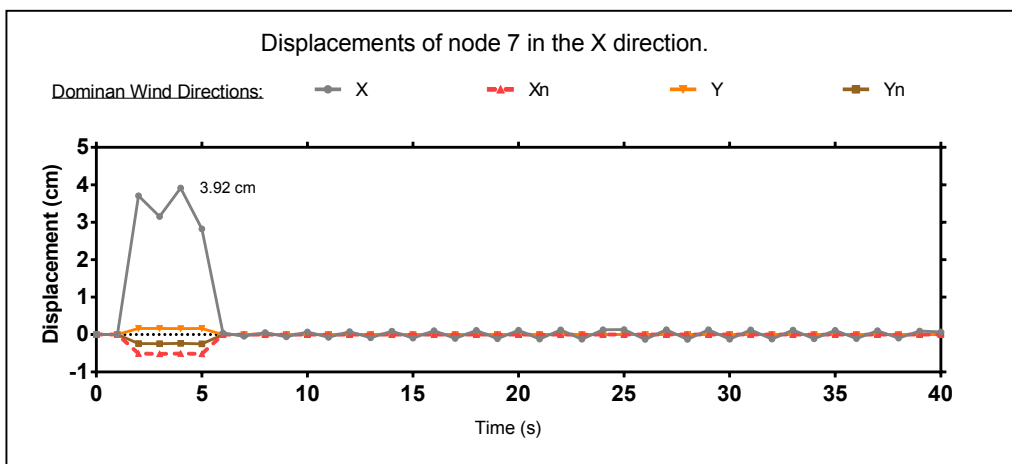


Fig. 14. Time-history record for displacements of node 7 in the X direction, load combination 1

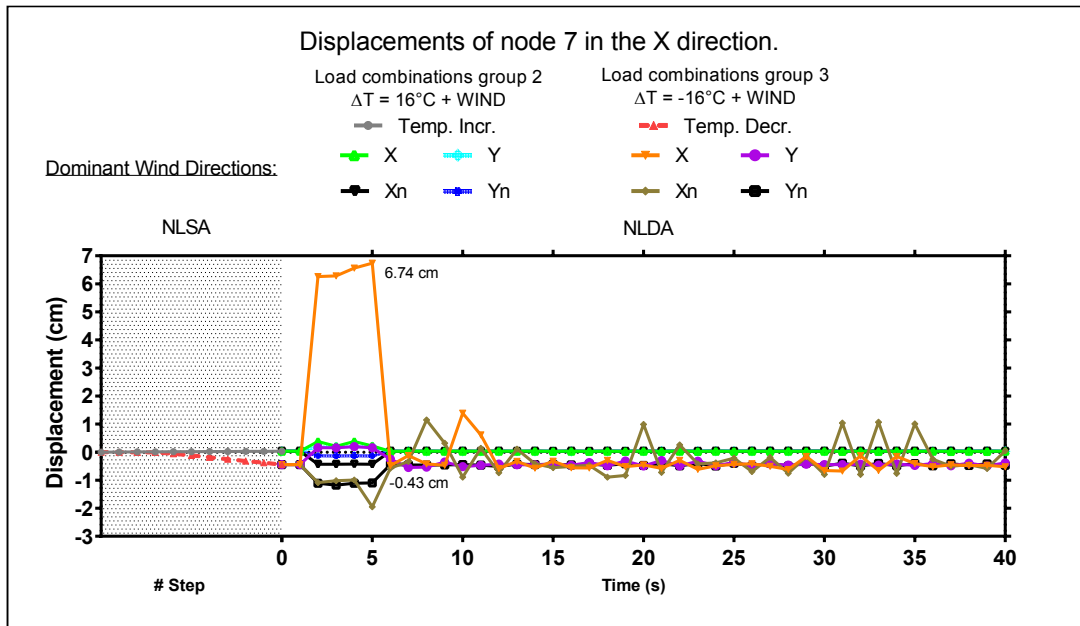


Fig. 15. Time-history record for displacements of node 7 in the X direction, load combination groups 2 and 3

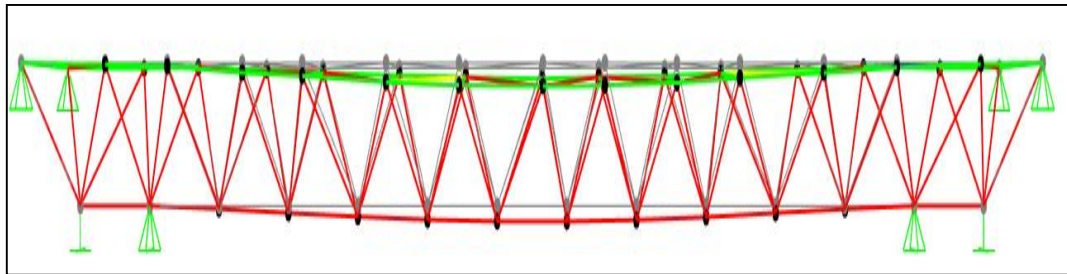


Fig. 16. SDLG vertical displacements (vertical scale 1:10)

Table 11. SDLG modal behavior

Mode	Frequency (Hz)	Period (s)
1	5.49	0.182
2	8.81	0.113
3	11.21	0.089
4	13.64	0.073
5	17.30	0.058
6	20.71	0.048
11	33.49	0.030

Table 13 shows the maximum internal forces of the SDLG. Due to the boundary conditions of pin-jointed systems, axial forces are predominant in the structure. It is observed that the existence of components associated with shear forces and bending moments is caused by the application of wind forces on the structure, however, its magnitude is low.

3.4 Coupling of Tensegrity Modules with the SDLG

In order to analyze the overall behavior of the superstructure, integrated by the SDLG and five X-T tensegrity modules, it is proposed to model the interaction of these systems, with the methodology mentioned in section 2.6, what is called in this work as system coupling. The coupling of systems consists in transmitting from one system to another, and vice versa, the mechanical effects resulting from sections 3.1 to 3.3, considering the boundary conditions defined for each structure.

On the one hand, reactions of the base nodes of the tensegrity system (see Table 14), are transmitted as point forces to the receiving nodes of the SDLG, in accordance to the configuration

shown in Fig. 2. These forces are considered as DL, applying the load combinations from Table 5. The results obtained by including the effects of the TS on the SDLG, show increases in the magnitude of the displacements of the system, since, in the horizontal direction, a displacement of -0.78 cm was registered, while in the vertical direction displacement reach a value of - 2.47 cm. However, the magnitude of these displacements does not suggest a radical change in the behavior of the SDLG, since the maximum increase is 0.13 cm in the Z direction.

Table 15 shows the maximum increments of axial forces produced by the tensegrity systems in the SDLG. In the first instance, it is observed that an increase of 16°C in temperature can produce an increment up to 1180 kg (4%) in the axial force of the elements of the top chord of the SDLG. In addition, the action of the wind in the Y direction on the X-T modules, together with an increase in temperature, induces a rise of 360 kg (2%) in the diagonal members. Similarly, when integrating the wind action in the X direction with

an increase or decrease in temperature, applied in the XT modules, axial force of the bottom chord elements is amplified to 950 kg (2%). Percent variations, belongs to the comparison against the results from Table 13.

On the other hand, the effects that the SDLG produces in the X-T modules are displacements of the support nodes 1, 4 and 6, which are shown in table 16. The largest displacement in the X direction is 0.514 cm, in the Y direction is 0.361 cm, and, in the Z direction it is -1.898 cm. This behavior is homogeneous in the SDLG system and with a similar magnitude in all load service combinations.

By including these displacements in the support nodes of the X-T module, additional forces are induced in the system, which are distributed to each of the elements. To analyze how the behavior of the X-T module is modified, a comparison between the axial forces obtained in sections 3.1 and 3.2 against the values resulting from the coupling of the systems is presented.

Table 12. SDLG maximum displacements

Service load case	DX (cm)	DY (cm)	DZ (cm)
2	-0.24	-0.24	0.18
3	-0.61	-0.62	-2.17
5 (DT = 0°C)	-0.28	-0.28	-0.93
5 (DT = 16°C)	-0.29	-0.31	-0.77
5 (DT = -16°C)	-0.29	-0.31	-1.10
6 (DT = 0°C)	-0.61	-0.62	-2.17
6 (DT = 16°C)	-0.62	-0.64	-2.00
6 (DT = -16°C)	-0.60	-0.64	-2.34

Table 13. SDLG maximum internal forces

Type of element	Axial force(Ton)	Shear force (Ton)		Flexural moment (Ton-m)		Location	Load case
		Y	Z	Y	Z		
Top chord	26.40	0.030	0.01	0.030	0.014	Extremes	6, $\Delta T = -16^\circ\text{C}$
	-19.20	-0.03	-0.01	-0.030	-0.014	Span center	6, $\Delta T = +16^\circ\text{C}$
Diagonal	13.28	0.03	0.01	0.03	0.010	Extremes	5, $\Delta T = -16^\circ\text{C}$
	-15.81	-0.04	-0.01	-0.039	-0.01	Extremes	6, $\Delta T = +16^\circ\text{C}$
Bottom chord	33.66	0.034	0.01	0.034	0.012	Span center	6, $\Delta T = -16^\circ\text{C}$
	-42.95	-0.03	-0.01	-0.034	-0.012	Extremes	6, $\Delta T = +16^\circ\text{C}$

Table 14. Maximum reactions at the base nodes of X-T module

Node	Fx (kg)	Fy (kg)	Fz (kg)
1	422	645	460
4	369	0	490
6	992	0	690

Table 15. SDLG maximum internal forces due coupling tensegrity systems

Type of element	Axial force (Ton)	Location	Load combination	Load case
Top chord	27.58	Extremes	CT-6	$\Delta T = 16^{\circ}\text{C}$
	-19.52	Span center	CT-6	$\Delta T = 16^{\circ}\text{C} + \text{WY}$
Diagonal	13.28	Extremes	CT-5	$\Delta T = -16^{\circ}\text{C}$
	-16.17	Extremes	CT-6	$\Delta T = 16^{\circ}\text{C} + \text{WYn}$
Bottom chord	34.39	Span center	CT-6	$\Delta T = -16^{\circ}\text{C} + \text{WX}$
	-43.90	Extremes	CT-6	$\Delta T = 16^{\circ}\text{C} + \text{WX}$

Table 16. Maximum displacements on the base nodes of the X-T module

Node	DX (cm)	DY (cm)	DZ (cm)
1	0.514	0.092	-1.898
4	0.137	0.361	-0.883
6	-0.464	-0.147	-0.504

When evaluating the behavior of the X-T module by only considering self-weight effects and the coupling of the systems, the force distribution shown in the Sw column of Tables 17 and 18 is presented. It is noted that the compression acting on the bar-type elements (Table 17), differs in a range from -4 to 0%, where the maximum decrement is 31 kg in bar 1. Regarding the type elements cable (Table 18), it is seen that, in the cables 7 to 25, the difference of axial forces on average is -1%, where the maximum variation is 19 kg (-4%) on cable 9. Cable 6 has an increase of 10%, while in the cables 26 and 27, there is a decrease of -98% and -100%, respectively. This indicates that cables 26 and 27 will enter a state of inactivity (slack) during the periods in which the SDLG is deformed up to the values in Table 16.

When considering the effects of wind from load combination 1, over the X-T module, in conjunction with the displacements of the support nodes caused by the coupling with the SDLG, the axial force distribution shown in column case 1 of Tables 17 and 18 is presented. From this analysis, variations from -1 to 0% in the compression received by the bar elements are observed (Table 17). In addition, the dominant wind direction that governs the behavior of each element is preserved. In the cable type elements (Table 18), differences from -3% to 5% in axial force are presented due to the coupling of the systems; with the exception of cable 26, where the variation is -29%. Cable 7 is the only element that shows a change in the dominant wind direction.

The differences in axial forces in the X-T module, once both systems are coupled, and by

considering a 16°C increase in temperature, are shown in the column Case 2, thermal effects, in Tables 17 and 18. For these load requirements, it can be observed that bar elements have higher order differences in the coupled case. Bar 3 is the most stressed element in the group, working under an axial force of 2,220 kg, equivalent to an increase of 679 kg.

In the cable elements (Table 18), increases in axial force are also exhibited. In cable 15 there is an increase of 473 kg (58%), which causes a total load of 1285 kg. In elements 18 and 19, the tension force increases 559 kg (83%) and 502 kg (91%), so these elements are subjected to a force of 1,235 and 1,054 kg, respectively. In contrast, for cables 6, 7 and 10, considerable differences are not identified, since the percentage increase in these elements ranges from -5 to 7%.

By integrating the temperature increases with the action of the wind, in the coupled system, the results of the case 2 column, Thermal + Wind effects, were obtained. Regarding the bar-elements, the bar 5 shows an increase of 672 kg (61%), working under a compression of 1,782 kg. However, the most stressed element is bar 3, where an axial force of 2,736 kg acts, which is 314 kg (13%) greater than that obtained before coupling the systems. Additionally, in bar 1, there is a change in the dominant wind direction of the element.

These loading conditions cause an equilibrium state where the largest increase occurring in the cable 15, since the tension increases 457 kg. Cable 18 undergo to the maximum tension forces for this load case as it works to a force of 1,444 kg. Elements 6, 7, 8, 14, 15 and 17 experience changes in the dominant wind direction that causes the maximum force in these elements.

Moreover, by inducing a 16°C decrease in temperature, once the X-T module is coupled with the SDLG, the force distributions of the case 3 column, Thermal effects, are generated. The

axial force of the bar elements is less than that generated by an increase in temperature (case 2). However, when compared against the forces before coupling, notable differences are perceived, since forces acting on these elements range from 365 kg to 497 kg. The increase of this magnitude implies percentage variations from 17 to 197%.

Regarding cable type elements, two main tendencies are observed. In the cables 7 to 10, 13, 26 and 27, the axial force is less than the values obtained without coupling systems. In elements 26 and 27 it is observed that they enter a period of inactivity, since the force decreases to 4 kg and 0 kg. The remaining cables have higher values compared to the point of comparison, where the largest increase is 200 kg in cable 18.

The inclusion of the effects of the wind with temperature decreases in the coupling of the X-T module produces the state of equilibrium of forces described in the case column 3, Thermal + Wind effects of Tables 17 and 18. For bar-like elements, it is observed that the differences in axial forces, originated when considering the effects of the coupling, are less than 117 kg, equivalent to -5% for bar 3. In this load condition, the dominant wind direction of bar 4 is modified.

For cable type elements, it was identified that the difference of greatest consideration occurs in cable 26, where the axial force decreases 314 kg (-90%). Cables 18 and 19 are the only elements where occur increases in the axial force, with a magnitude of 98 kg and 94 kg. In the remaining elements, axial force variations are from an order of +/- 50 kg. In cables 6, 26 and 27, modifications in the dominant wind direction were identified.

In addition to the registered axial force variations in the components of the X-T module, differences

related to the direction and magnitude of the nodal displacements are identified. Table 19 shows the displacements of each node, resulting from the coupling of the X-T module and the wind effects from load combinations 1, 2.b and 3.b.

In the load combination 1, it is highlighted a displacement decrease in the X direction, with a value of -0.13 cm. In the Y and Z directions it is noted a slight increase in the magnitude of the displacements, equal to 0.62 cm and 0.11 cm, respectively. Furthermore, a change occurs in the wind direction that produces the largest displacements.

The nodal movements produced by the union of the systems, associated to the load combination 2.b, report displacement differences of -0.33 cm. For the free nodes, increases of up to 0.91 cm in the Y direction, and, 1.05 cm for the Z direction, are distinguished. In this group of nodes (with the exception of node 6), changes in the dominant wind direction occur.

From the results corresponding to the coupling of systems with the loading conditions of case 3.b, it is observed that, due to the distribution of forces that occur in the system under these conditions, leads to the reduction of displacements of - 1.15 cm on average. In node 7 the displacements are reduced to -1.66 cm. Unlike the previous cases, the dominant wind directions that produce maximum displacements are not altered.

In particular, the displacements of the support nodes 1, 4 and 6 were evaluated, since they exhibit a different behavior from that of the free nodes. Both node 4 and node 6, have freedom of movement in the Y direction, therefore, in load combination 1, there are increases of 0.35 cm and 1.40 cm, respectively. For the load

Table 17. Maximum axial compression forces of bar elements for self-weight analysis for the load combination groups 1, 2 and 3, due coupling X-T modules with SDLG

Sw.	Load comb. 1 (DT=0°C)			Load comb. group 2 (DT=+16°C)			Load comb. group 3 (DT=-16°C)		
	Wind effects			Thermal effects			Thermal + Wind effects		
Bar	Axial force(kg)	Axial force(kg)	WDD	Axial forc (kg)	Axial force(kg)	WDD	Axial force(kg)	Axial force(kg)	WDD
1	1024	1367	Yn	1678	2141	Xn	497	1328	X
2	806	1030	Y	1669	1883	Y	397	1034	X
3	773	2439	X	2220	2736	X	366	2240	X
4	639	1008	Xn	1412	1780	Xn	209	866	Y
5	417	1080	X	1595	1782	Xn	365	1197	X

Table 18. Maximum axial tension forces of cable elements for self-weight analysis for the load combination groups 1, 2 and 3, due coupling X-T modules with SDLG

Cable	Sw.	Load comb. 1 (DT=0°C)			Load comb. group 2 (DT=+16°C)			Load comb. group 3 (DT=-16°C)		
		Wind effects			Thermal effects	Thermal + Wind effects		Thermal effects	Wind effects	
	Axial force(kg)	Axial force(kg)	WDD	Axial force(kg)	Axial force(kg)	WDD	Axial force(kg)	Axial force(kg)	WDD	
6	517	698	Y	837	1018	Y	209	275	X	
7	486	662	Yn	775	980	Yn	165	664	X	
8	445	608	Xn	448	658	Yn	126	303	Xn	
9	486	659	X	845	979	X	176	672	X	
10	262	597	X	422	587	X	14	386	X	
11	377	654	X	813	911	Xn	73	423	X	
12	369	631	X	779	868	Xn	65	399	X	
13	279	620	X	420	594	X	2	374	X	
14	292	560	X	861	935	Xn	192	620	X	
15	410	859	X	1285	1407	Xn	299	949	X	
16	124	496	X	723	865	Y	165	551	X	
17	71	362	X	543	649	Xn	114	405	X	
18	290	1184	X	1235	1444	X	276	1303	X	
19	216	1098	X	1054	1327	X	217	1213	X	
20	164	555	Xn	468	847	Xn	113	539	Xn	
21	182	583	Xn	533	919	Xn	128	568	Xn	
22	76	281	Xn	260	456	Xn	67	281	Xn	
23	95	327	Xn	325	544	Xn	84	323	Xn	
24	145	626	X	595	748	X	125	672	X	
25	112	502	X	479	597	X	96	535	X	
26	4	181	Y	4	181	Y	4	33	X	
27	0	200	Yn	0	201	Yn	0	86	Yn	

Table 19. Maximum nodal displacements for the load combinations 1, 2b and 3b, due coupling of systems

Node	Case 1 (DT=0°C)				Case 2.b (DT=+16°C)				Case 3.b (DT=-16°C)			
	Wind effects				Thermal + Wind effects				Thermal + Wind effects			
	DX (cm)	DY (cm)	DZ (cm)	DWD	DX (cm)	DY (cm)	DZ (cm)	DWD	DX (cm)	DY (cm)	DZ (cm)	DWD
2	3.1	-0.2	0.18	X	-0.75	0.06	-0.07	Xn	4.32	-0.35	0.3	X
3	3.17	-0.13	-0.13	X	-0.76	-0.08	0.02	Xn	4.35	-0.1	-0.13	X
4	-	-0.4	-	Yn	-	-0.05	-	Yn	-	-0.1	-	Yn
5	2.56	-0.29	0.61	X	-0.77	-0.18	0.1	X	3.67	-0.38	0.9	X
6	-	-1.47	-	Xn	-	-2.12	-	Xn	-	-2.11	-	Yn
7	3.74	-0.78	0.87	X	0.45	-1.12	1.26	Xn	5.08	-1.29	1.21	X
8	3.51	-0.78	0.97	X	-0.81	-1.12	-1.17	Xn	4.8	-1.29	1.29	X
9	1.51	-0.08	1.14	X	-0.43	0.02	-0.29	Xn	2.09	-0.06	1.53	X
10	1.84	-1.3	-0.38	X	-0.54	-0.74	0.14	Xn	2.54	1.77	-0.56	X

combination 2.b, the magnitude of the displacement of node 4 is decreased by -0.13 cm. However, node 6, the maximum variation of 1.99 cm is presented, which implies a displacement of 2.12 cm. Similarly, at the combination 3.b, in node 4 there is a decrease of -0.24 cm, and node 6 shows an increase of 1.85 cm.

4. DISCUSSION

From this work, it is highlighted as a discussion that the results obtained show congruence and extend what was reported by the research of Ashwear and Eriksson [13], and with those of Lazzari et al. [5].

The research of Ashwear and Eriksson [13], is oriented in to the study of 2D tensegrity systems under temperature variations, associated with temperature decreases of 45°C and increments of 26°C. It is reported that, according to the boundary conditions of the support nodes, and, the relationship between the coefficient of thermal expansion of the bars with that of the cables, the behavior of the assembly can be described by one of the categories shown in Table 20.

Considering the boundary conditions of the X-T module, which has one articulated support (fixed to movement) node and two other supports with freedom of movement only in the Y direction; in addition, to a relationship of thermal expansion coefficients expressed as $\alpha_b > \alpha_c$, it can be observed that behavior of the X-T module matches with one the categories from Table 20. However, it is noted that when performing analysis of a 3D tensegrity system, additional features are identified to those reported by Ashwear and Eriksson [13].

Although, the overall behavior of the structural system is acts accordance with previously described work, it is observed that, at an increase in temperature, the axial force of some elements may decrease, while, under a decrease in temperature, the axial force of certain elements increases. This phenomenon occurs, due to the fact that the spatial position of the X-T module, under the thermal variations studied, implies that the nodes that define elements 26 and 27 approach or move away, which causes increases or decreases in axial force.

In the research of Lazzari et al. [5] quasi-static analyzes of the effects of wind on the roof of the La Plata stadium were performed. The wind was considered as random points for a time of 40 s, representing the stochastic nature of the wind, with a logarithmic behavior. From their results, it is emphasized that by using this methodology it was feasible to identify the maximum nodal

displacements and the highest stresses for bars and cables. In addition, it was identified that on some cable elements the tensile forces are reduced to a null value, when wind acts in a specific direction.

This behavior is consistent with the results obtained in this investigation, since, due to the conditions and the asymmetry of the assembly, each element is governed by a specific wind direction. The advantage of using dynamic models is that they allow to evaluate the behavior of the system when is loaded and in the free vibration period, which is used to determine, in a simple way, the stability of the assembly.

The most drastic effects implied by the coupling of the five X-T modules with the SDLG, are the increases in node displacements and in the axial forces of the structural elements. It was recorded a movement of 2.12 cm for node 6, which must be considered when designing the base node connection devices. Additionally, compression force in bar 3 rises up to 2,736 kg, while, tension in cable 18 reaches a value of 1,444 kg. These axial forces determine the cross-section of each type of elements.

It is important to highlight the following discussions about the proposed methodology for the coupling of the systems. SDLG is a system that presents a linear behavior within the elastic range. Therefore, it is feasible to use the principle of superposition, to transmit the loads generated by the tensegrity systems. This allowed to calculate the displacements and the forces developed in the SDLG.

However, for the X-T module, although its components remain within the elastic range, the system is intrinsically non-linear and manifests large displacements, so that the principle of effect superposition is not suitable for modeling the coupling. Therefore, the proposed method to determine with greater approximation, the axial forces and the nodal movements, which occur in

Table 20. Structural behavior of 2D tensegrity systems under environment temperature variations (adapted from Ashwear and Eriksson [13])

Thermal expansion coefficient relations	Boundary conditions of bar and cable elements' nodes		
	Fixed - Free	Fixed - Fixed	Fixed – Fixed (Supports)
$ab = ac$	No variation		
$ab < ac$	Temp. increase → Axial force reduces	Temp. decrease → Axial force rises	Temp. increase → Axial force rises
$ab > ac$	Temp. increase → Axial force rises	Temp. decrease → Axial force reduces	Temp. decrease → Axial force reduces

the X-T module, due to the coupling, was through non-linear dynamic models, representing the maximum displacements of the SDLG, as a base movement dynamic problem. The limitation of implementing these methods is that the modal behavior of the complete assembly is unknown.

5. CONCLUSION

By means of non-linear static analyses, it was feasible to define the boundary conditions for the base node of the X-T module, which allows to couple the TS with the SDLG. Restricting the degrees of freedom in the vertical direction (Z direction) and in the transverse direction (X direction) reduces the displacements of the support nodes of the X-T module, thereby preserving the internal area designated for the pedestrian crossing. In addition, it allows the system to distribute the internal forces evenly and the assembly to continue working according to the mechanical principles of the tensegrity structures, that is, that the bar-like elements work only under compression and the cables under tensile forces.

Through static analyzes of the SDLG, and non-linear dynamic analyses of TS, the internal forces and the structural response were obtained, generated by the integration of wind effects and variations of temperature in each system.

The methodology used to develop the coupling of the tensegrity modules with the superstructure of the pedestrian bridge, allowed to determine the effects caused by the interaction of both systems. As well as maximum displacements and internal forces in each system. Through this methodology, the characteristics necessary to generate the connection devices were defined, according to the idealizations made in the finite element models. Through this methodology the necessary conditions to generate the connection devices were defined, according to the idealizations made in the finite element models.

From the non-linear dynamic analysis performed for the X-T module, it is denoted the capacity of this system to return to its initial equilibrium state, once the excitation period is over. The ability of the X-T module to return to the initial equilibrium state is highlighted, once the excitation period is over. This fact allows to define that the generated tensegrity system shows a stable behavior under the proposed working conditions.

When determining the maximum axial force in each member of the module, the geometric cross

sections were defined, which ensure a behavior in the elastic range of each element, and thus avoid exceeding the critical load that would cause instability in the system, as effects buckling in the bar elements; while, yielding and rupture are avoided in cables.

ACKNOWLEDGEMENTS

Authors acknowledge the support of the Autonomous University of Queretaro (UAQ), as well The Mexican Council of Science & Technology (CONACYT).

COMPETING INTERESTS

Authors have declared that no competing interests exist.

REFERENCES

1. Jáuregui Gómez V. Tensegrity structures and their application to architecture. 2004;1–239.
2. Bel Hadj Ali N, Rhode-Barbarigos L, Pascual Albi AA, Smith IFC. Design optimization and dynamic analysis of a tensegrity-based footbridge. *Eng. Struct.* 2010;32(11):3650–3659.
3. De Boeck J. Tensegrity bridges. Delft University of Technology; 2013.
4. Motro R, Raducanu V, Fuller RB. Tensegrity systems. 2003;18(2):77–84.
5. Lazzari M, Vitaliani RV, Majowiecki M, Saetta AV. Dynamic behavior of a tensegrity system subjected to follower wind loading. *Comput. Struct.* 2003; 81(22–23):2199–2217.
6. Australian Steel Institute. Kurilpa Bridge, Brisbane Structural Engineering Award 2010 (Qld); 2010.
7. Korkmaz S, Ali NBH, Smith IFC. Self-repair of a tensegrity pedestrian bridge through grouped actuation. *Proc. Int. Conf. Comput. Civ. Build. Eng. Nottingham, UK.* 1987;449:2010.
8. Chen LH, et al. Soft spherical tensegrity robot design using rod-centered actuation and control. *J. Mech. Robot.* 2017;9(2).
9. Tran HC, Lee J. Geometric and material nonlinear analysis of tensegrity structures. *Acta Mech. Sin. Xuebao.* 2011;27(6):938–949.
10. Murakami H. Static and dynamic analyses of tensegrity structures. Part 1. Nonlinear equations of motion. *Int. J. Solids Struct.* 2001;38(20):3599–3613.

11. Murakami H. Static and dynamic analyses of tensegrity structures. Part II. Quasi-static analysis. *Int. J. Solids Struct.* 2001;38(20):3615–3629.
12. Lu CJ, Wang XD, Lu SN. Wind-induced dynamic analysis of the flat tensegrity structures in time domain. *Appl. Mech. Mater.* 2012;166–169:140–143.
13. Ashwear N, Eriksson A. Influence of temperature on the vibration properties of tensegrity structures. *Int. J. Mech. Sci.* 2015;99:237–250.
14. Zhang Z, Dong S, Fu X. Structural design of a spherical cable dome with stiff roof. *Int. J. Sp. Struct.* 2007;22(3):45–56.
15. Rhode-Barbarigos L, Hadj Ali NB, Motro R, Smith IFC. Tensegrity modules for pedestrian bridges. *Eng. Struct.* 2010;32(4):1158–1167.
16. Tibert AG, Pellegrino S. Review of form-finding methods for tensegrity structures. *Int. J. Sp. Struct.* 2011;26(3):241–255.
17. Gomez Estrada G. Analytical and numerical investigations of form-finding methods for tensegrity structures. 2007;152.
18. Yuan X, Chen L, Dong S. Prestress design of cable domes with new forms. *Int. J. Solids Struct.* 2007;44(9):2773–2782.
19. Ochoa Peralta LA, Orellana Ochoa PF. Tensegriedad como sistema estructural alternativo aplicado a cubiertas. Universidad de Cuenca; 2017.
20. Cobos JI. Tensegriedad como sistema estructural alternativo aplicado a puentes peatonales. UNIVERSIDAD DE CUENCA; 2018.
21. Connelly R. Globally rigid symmetric tensegrities tensegrites symetriques globalement rigides. *Struct. Topol.* 1995;21:59–78.
22. Connelly R, Whiteley W. Second-order rigidity and prestress stability for tensegrity frameworks. *SIAM J. Discret. Math.* 1996;9(3):453–491.
23. Deng H, Kwan ASK. Unified classification of stability of pin-jointed bar assemblies. *Int. J. Solids Struct.* 2005;42(15):4393–4413.
24. Zhang JY, Ohsaki M. Stability conditions for tensegrity structures. *Int. J. Solids Struct.* 2007;44(11–12):3875–3886.
25. Lazopoulos KA. Stability of an elastic tensegrity structure. *Acta Mech.* 2005; 179(1–2):1–10.
26. Amendola A, Carpentieri G, de Oliveira M, Skelton RE, Fraternali F. Experimental investigation of the softening-stiffening response of tensegrity prisms under compressive loading. *Compos. Struct.*; 2014.
27. Zhang L, Zhang C, Feng X, Gao H. Snapping instability in prismatic tensegrities under torsion. *Appl. Math. Mech. (English Ed.)* 2016;37(3):275–288.
28. Atig M, El Ouni MH, Ben Kahla N. Dynamic stability analysis of tensegrity systems. *Eur. J. Environ. Civ. Eng.* 2017;8189:1–18.
29. Secretaria de Comunicaciones y Transportes. N·PRY·CAR·6·01·003/01 Cargas y Acciones. In *Proyectos de Nuevos Puentes y Estructuras Similares.* 2001;1–25.
30. ASTM International, ASTM A500 / A500M-18, Standard Specification for Cold-Formed Welded and Seamless Carbon Steel Structural Tubing in Rounds and Shape. West Conshohocken, PA: ASTM International; 2018.
31. ASTM International, ASTM A53 / A53M-18, Standard Specification for Pipe, Steel, Black and Hot-Dipped, Zinc-Coated, Welded and Seamless. West Conshohocken, PA: ASTM International; 2018.
32. González-Martínez ÁO, Horta-Rangel JM, Pérez-Lara-y-Hernández MÁ, Arroyo-Contreras GM. Análisis de un puente peatonal conformado por una estructura soportante en forma de triditrabe y acoplada a módulos presforzados tipo tensegrity. *Perspect. la Cienc. y la Ing.* 2019;2. In Press. Spanish
33. ASTM International, ASTM B429 / B429M-10e1, Standard Specification for Aluminum-Alloy Extruded Structural Pipe and Tube (Withdrawn 2019). West Conshohocken, PA: ASTM International; 2010.
34. ASTM International, ASTM A586-18, Standard Specification for Metallic-Coated Parallel and Helical Steel Wire Structural Strand. West Conshohocken, PA: ASTM International; 2018.
35. Pellegrino S, Calladine CR. Matrix analysis of statically and kinematically indeterminate frameworks. *Int. J. Solids Struct.* 1985;22:409–428.
36. Calladine CR, Pellegrino S. First-order infinitesimal mechanisms. *Int. J. Solids Struct.* 1991;27(4):505–515.
37. Gurtin ME. *An Introduction to continuum mechanics.* New York: Academic Press; 1981.

38. Kebiche K, Kazi-Aoual MN, Motro R. Geometrical non-linear analysis of tensegrity systems. *Eng. Struct.* 1999;21(9):864–876.
39. Cook RD, Malkus DS, Plesha ME, Witt RJ. *Concepts and Applications of finite element analysis.pdf*. Wisconsin: John Wiley & Sons, INC; 2002.
40. Marin M. An uniqueness result for body with voids in linear thermoelasticity. *Rend. di Mat.* 1997;17(7):103–113.
41. Marin M, Brasov UT. On the domain of influence in thermoelasticity of bodies with voids *archivum mathematicum*. *Arch. Math.* 1997;33(3):301–308.
42. Marin M. An evolutionary equation in thermoelasticity of dipolar bodies. *J. Math. Phys.* 1999;40(3):1391–1399.
43. Cook RD, Saunders H. *Concepts and applications of finite element analysis*. 2009;106(1).
44. Craig RRJ, Kurdila AJ. *Fundamentals of Structural Dynamics*. John Wiley & Sons; 2011.
45. Clough RW, Penzien J. *Dynamics of structures*. Computers & Structures, Inc.; 1995.
46. SAP2000. *Computers & Structures, Inc.* [Online]. Available: <https://www.csiespana.com/software/2/sap2000>
47. Secretaria de Comunicaciones y Transportes. N·PRY·CAR·6·01·004/01 Viento. In *Proyectos de Nuevos Puentes y Estructuras Similares*. 2001;1–18.
48. INEGI. [Online]. Available: <http://cuentame.inegi.org.mx/mografias/informacion/queret/territorio/clima.aspx?tema=me&e=22>
49. AASHTO. *Guide specifications for design of pedestrian bridges*. 2009;40.

© 2019 Martínez et al.; This is an Open Access article distributed under the terms of the Creative Commons Attribution License (<http://creativecommons.org/licenses/by/4.0>), which permits unrestricted use, distribution, and reproduction in any medium, provided the original work is properly cited.

Peer-review history:
The peer review history for this paper can be accessed here:
<https://sdiarticle4.com/review-history/52005>